

# Imaging complex structures with diffuse light

Soren D. Konecky<sup>1</sup>, George Y. Panasyuk<sup>2</sup>, Kijoon Lee<sup>1,3</sup>, Vadim Markel<sup>2,4</sup>, Arjun G. Yodh<sup>1</sup>, John C. Schotland<sup>2</sup>

1. Department of Physics and Astronomy, University of Pennsylvania, Philadelphia, PA 19104-6396

2. Department of Bioengineering, University of Pennsylvania, Philadelphia, PA 19104-6396

3. Division of Bioengineering, Nanyang Technological University, Singapore 637457

4. Department of Radiology, University of Pennsylvania, Philadelphia, PA 19104-6396

[Correspondence to: Soren D. Konecky \(Email: skonecky@physics.upenn.edu\)](mailto:skonecky@physics.upenn.edu)

**Abstract:** We use diffuse optical tomography to quantitatively reconstruct images of complex phantoms with millimeter sized features located centimeters deep within a highly-scattering medium. A non-contact instrument was employed to collect large data sets consisting of greater than  $10^7$  source-detector pairs. Images were reconstructed using a fast image reconstruction algorithm based on an analytic solution to the inverse scattering problem for diffuse light.

© 2008 Optical Society of America

**OCIS codes:** (110.0113) Imaging through turbid media; (170.3880) Medical and biological imaging

---

## References and links

1. M. C. W. van Rossum and T. M. Nieuwenhuizen, "Multiple scattering of classical waves: microscopy, mesoscopy and diffusion," *Rev. Mod. Phys.* **71**, 313–371 (1999).
2. A. Yodh and B. Chance, "Spectroscopy and imaging with diffuse light," *Phys. Today* pp. 34–40 (1995).
3. S. R. Arridge, "Optical tomography in medical imaging," *Inverse Problems* **15**, R41–R93 (1999).
4. A. P. Gibson, J. C. Hebden, and S. R. Arridge, "Recent advances in diffuse optical imaging," *Phys. Med. Biol.* **50**, R1–R43 (2005).
5. S. B. Colak, M. B. van der Mark, G. W. Hooft, J. H. Hoogenraad, E. S. van der Linden, and F. A. Kuijpers, "Clinical optical tomography and NIR spectroscopy for breast cancer detection," *IEEE J. Sel. Top. Quantum Electron.* **5**, 1143–1158 (1999).
6. D. J. Hawrysz and E. M. Sevick-Muraca, "Developments toward diagnostic breast cancer imaging using near-infrared optical measurements and fluorescent contrast agents," *Neoplasia* **2**, 388–417 (2000).
7. Y. Xu, X. J. Gu, L. L. Fajardo, and H. B. Jiang, "In vivo breast imaging with diffuse optical tomography based on higher-order diffusion equations," *Appl. Opt.* **42**, 3163–3169 (2003).
8. J. P. Culver, R. Choe, M. J. Holboke, L. Zubkov, T. Durduran, A. Slempt, V. Ntziachristos, B. Chance, and A. G. Yodh, "Three-dimensional diffuse optical tomography in the parallel plane transmission geometry: Evaluation of a hybrid frequency domain/continuous wave clinical system for breast imaging," *Med. Phys.* **30**, 235–247 (2003).
9. Q. I. Zhu, M. M. Huang, N. G. Chen, K. Zarfos, B. Jagjivan, M. Kane, P. Hedge, and S. H. Kurtzman, "Ultrasound-guided optical tomographic imaging of malignant and benign breast lesions: Initial clinical results of 19 cases," *Neoplasia* **5**, 379–388 (2003).
10. X. Intes, J. Ripoll, Y. Chen, S. Nioka, A. G. Yodh, and B. Chance, "In vivo continuous-wave optical breast imaging enhanced with Indocyanine Green," *Med. Phys.* **30**, 1039–1047 (2003).
11. A. Li, E. L. Miller, M. E. Kilmer, T. J. Brukilacchio, T. Chaves, J. Stott, Q. Zhang, T. Wu, M. Chorlton, R. H. Moore, D. B. Kopans, and D. A. Boas, "Tomographic optical breast imaging guided by three-dimensional mammography," *Appl. Opt.* **42**, 5181–5190 (2003).
12. S. D. Jiang, B. W. Pogue, T. O. McBride, M. M. Doyley, S. P. Poplack, and K. D. Paulsen, "Near-infrared breast tomography calibration with optoelastic tissue simulating phantoms," *J. Electron. Imaging* **12**, 613–620 (2003).
13. D. A. Benaron, J. van Houten, D. C. Ho, S. D. Spilman, and D. K. Stevenson, "Imaging neonatal brain injury using light-based optical tomography," *Pediatr. Res.* **35**, A378–A378 (1994).

14. J. P. van Houten, W. F. Cheong, E. L. Kermit, T. R. Machold, D. K. Stevenson, and D. A. Benaron, "Clinical measurement of brain oxygenation and function using light-based optical tomography," *Pediatr. Res.* **39**, 2273–2273 (1996).
15. A. Y. Bluestone, G. Abdoulaev, C. H. Schmitz, R. L. Barbour, and A. H. Hielscher, "Three-dimensional optical tomography of hemodynamics in the human head," *Opt. Express* **9**, 272–286 (2001).
16. G. Strangman, D. A. Boas, and J. P. Sutton, "Non-invasive neuroimaging using near-infrared light," *Biol. Psychiatry* **52**, 679–693 (2002).
17. J. C. Hebden, A. Gibson, R. M. Yusof, N. Everdell, E. M. C. Hillman, D. T. Delpy, S. R. Arridge, T. Austin, J. H. Meek, and J. S. Wyatt, "Three-dimensional optical tomography of the premature infant brain," *Phys. Med. Biol.* **47**, 4155–4166 (2002).
18. J. C. Hebden, "Advances in optical imaging of the newborn infant brain," *Psychophysiology* **40**, 501–510 (2003).
19. J. P. Culver, A. M. Siegel, J. J. Stott, and D. A. Boas, "Volumetric diffuse optical tomography of brain activity," *Opt. Lett.* **28**, 2061–2063 (2003).
20. A. M. Siegel, J. P. Culver, J. B. Mandeville, and D. A. Boas, "Temporal comparison of functional brain imaging with diffuse optical tomography and fMRI during rat forepaw stimulation," *Phys. Med. Biol.* **48**, 1391–1403 (2003).
21. G. Q. Yu, T. Durduran, D. Furuya, J. H. Greenberg, and A. G. Yodh, "Frequency-domain multiplexing system for in vivo diffuse light measurements of rapid cerebral hemodynamics," *Appl. Opt.* **42**, 2931–2939 (2003).
22. J. C. Schotland, "Continuous wave diffusion imaging," *J. Opt. Soc. Am. A* **14**, 275–279 (1997).
23. V. A. Markel and J. C. Schotland, "Inverse scattering for the diffusion equation with general boundary conditions," *Phys. Rev. E* **64**, R035,601 (2001).
24. V. A. Markel and J. C. Schotland, "The inverse problem in optical diffusion tomography. II. Inversion with boundary conditions," *J. Opt. Soc. Am. A* **19**, 558–566 (2002).
25. V. A. Markel and J. C. Schotland, "Effects of sampling and limited data in optical tomography," *Appl. Phys. Lett.* **81**, 1180–1182 (2002).
26. J. C. Schotland and V. A. Markel, "Inverse scattering with diffusing waves," *J. Opt. Soc. Am. A* **18**, 2767–2777 (2001).
27. G. Turner, G. Zacharakis, A. Soubret, J. Ripoll, and V. Ntziachristos, "Complete-angle projection diffuse optical tomography by use of early photons," *Opt. Lett.* **30**, 409–411 (2005).
28. R. Schulz, J. Ripoll, and V. Ntziachristos, "Noncontact optical tomography of turbid media," *Opt. Lett.* **28**, 1701–1703 (2003).
29. Z.-M. Wang, G. Y. Panasyuk, V. A. Markel, and J. C. Schotland, "Experimental demonstration of an analytic method for image reconstruction in optical tomography with large data sets," *Opt. Lett.* **30**, 3338–3340 (2005).
30. V. A. Markel, V. Mital, and J. C. Schotland, "The inverse problem in optical diffusion tomography. III. Inversion formulas and singular value decomposition," *J. Opt. Soc. Am. A* **20**, 890–902 (2003).
31. V. A. Markel and J. C. Schotland, "Symmetries, inversion formulas and image reconstruction for optical tomography," *Phys. Rev. E* **70**, 056,616 (2004).
32. R. Choe, "Diffuse Optical Tomography and Spectroscopy of Breast Cancer and Fetal Brain," Ph.D. thesis, University of Pennsylvania (2005).
33. A. Ishimaru, *Wave Propagation and Scattering in Random Media* (IEEE Press, Piscataway, NJ, 1997).
34. R. Aronson, "Boundary conditions for diffuse light," *J. Opt. Soc. Am. A* **12**, 2532–2539 (1995).

---

## 1. Introduction

The study of light propagation in highly scattering random media such as clouds, paint and tissue is of fundamental interest and considerable applied importance [1]. Novel physical effects such as the dynamic correlations of speckle patterns and weak localization arise from coherent effects in multiple scattering. Incoherent effects are also of interest and have led to new experimental tools to probe the structure of highly-scattering media. One such technique, known as diffuse optical tomography (DOT), uses highly scattered near-infrared light to image biological tissue and provide functional information about physiological parameters such as blood volume and oxygenation [2–4]. Current clinical applications of DOT include breast imaging [5–12] and functional brain mapping [13–21].

In an optically-thick medium such as the human breast, multiple scattering of light creates a fundamental obstruction to the direct formation of images. DOT overcomes this problem to some extent by solving an appropriate inverse problem, usually based on the diffusion equation, wherein the optical properties of a highly-scattering medium are reconstructed from boundary measurements. Since such inverse scattering problems are severely ill-posed [3], the resultant

image quality in DOT is expected to be poor; typical images resemble structureless ‘blobs’. As a result many accept that anatomically accurate DOT images cannot be reconstructed. Accordingly, the emphasis in DOT has been on functional imaging, and on multi-modality imaging, in which simultaneously acquired MRI or CT images are used to provide anatomical detail [4].

It has been suggested that the relatively low quality of images in DOT can be improved by the use of large data sets [22–26]. Moreover, data sets of approximately  $10^8$  measurements may be readily acquired with non-contact DOT systems [27–29]. For example, Turner et al. have shown that simple shapes can be imaged in an experiment using an *optically-thin* sample by employing time gating of early-arriving photons [27]. However, this approach uses photons that travel ballistically through the sample and is therefore not useful in optically thick tissues such as breast and brain.

In this contribution, we demonstrate for the first time that three-dimensional, quantitative images of the interior of such an optically thick medium, with millimeter scale complex structure, can be acquired using DOT. The reconstructed images exhibit spatially-resolved features that are much smaller than the overall size of the sample and are obtained by utilizing large data sets and fast image reconstruction algorithms developed in earlier work [23–26, 30, 31]. Our findings have important implications for biomedical applications, since we achieve image quality and spatial resolution sufficient for visualization of anatomical detail.

We have applied fast reconstruction methods to DOT imaging in previous work [29]. However, in that work we imaged a sample with very strong absorption and a simple geometrical structure (i.e. two perfectly absorbing balls). This choice did not allow us to explore the full potential of large data sets and is of limited relevance to conditions encountered in tissue. The experimental reconstructions obtained in Ref. [29] appeared as spherical inhomogeneities correctly positioned in space, but slightly larger than the actual balls. Thus the detection and localization of targets was shown, but neither the ability to reconstruct the shapes of spatially extended objects nor the ability to image objects with more biologically realistic absorption contrast was demonstrated. To overcome these limitations, in the present work we have reconstructed images of several objects that have complex structure and have optical properties comparable to those of tissue. Experiments with these objects immersed in an optically-thick medium reveal that DOT is capable of producing quantitative images of complex structures with spatially-resolved features on the sub-centimeter scale. This level of detail and the spatial resolution achieved in our experiment are expected to significantly enhance the practical utility of DOT, especially for localization and demarcation of breast tumors. We have quantified the maximum attainable resolution with the current experimental system, and we have demonstrated the effects of sampling on image quality. The effect of noise on the practical limits of diffuse optical experimental resolution was also characterized.

## 2. Methods

### 2.1. Instrumentation

The experimental apparatus consisted of a continuous-wave diode laser (Model TC40, SDL Inc., San Jose, CA) operating at 785 nm and coupled via a 100  $\mu\text{m}$  multi-mode fiber to a pair of galvanometer-controlled mirrors (Innovations in Optics, Woburn, MA). The mirrors raster scanned the beam (on a  $35 \times 35$  rectangular grid with 4 mm step size) over a  $13.6 \times 13.6$   $\text{cm}^2$  square on one side of an imaging tank containing a target. For each laser beam position, the light transmitted through the tank was collected by a  $f=25$  mm F/0.95 lens and focused on a front-illuminated thermoelectric-cooled 16-bit CCD array (DV887ECS-UV, Andor Technology, Belfast, Ireland). A  $20 \times 20$   $\text{cm}^2$  square area of the opposite surface was mapped onto a square grid of  $512 \times 512$  CCD pixels; this corresponds to a grid of detectors with 0.4 mm step. The signal recorded by each CCD pixel for a given source beam position defined an in-

dependent measurement. The total size of the data set recorded in a single experiment was  $(35 \times 512)^2 \approx 3 \times 10^8$ . Somewhat smaller subsets of the data were used for image reconstruction.

The imaging tank had an inner thickness  $L = 6$  cm, and was filled with a mixture of water, a highly scattering fat emulsion (Liposyn III, 30%, Abbott Laboratories, Chicago, IL), and India ink (Black India 4415, Sanford, Bellwood, IL). The absorption and the reduced scattering coefficients of the mixture at 786 nm were  $\mu_a = 0.05$  cm<sup>-1</sup> and  $\mu'_s = 7.5$  cm<sup>-1</sup>, respectively. The transport mean free path was  $\ell^* = 1/(\mu_a + \mu'_s) \approx 1.3$  mm. The diffuse wave number (i.e. the inverse characteristic length over which the diffuse waves decay exponentially) was  $k_d \approx \sqrt{3\mu_a/\ell^*} \approx 1.1$  cm<sup>-1</sup>. The tank thickness was therefore much larger than  $\ell^*$ , and thus the experiments were carried out in the diffusion regime. In addition  $k_d L \approx 6.6$ , and thus the transmitted light was substantially attenuated. These parameters are typical of human breast tissues in the NIR spectral region.

## 2.2. Targets

Targets were made of a mixture of silicone rubber (RTV-12, General Electric, Waterford, NY), titanium dioxide (T-8141, Sigma-Aldrich, St. Louis, MO), and carbon black (Raven 5000 Ultra Powder II, Columbian Chemicals Co., Marietta, GA) [32]. The ingredients were mixed in a proportion such that the reduced scattering coefficient of the targets was approximately matched to that in the surrounding fluid while the absorption coefficient  $\mu_a$  was four times larger. Targets were made in the shape of letters (3 cm tall, 2 cm wide, 5 mm thick with individual components 3 mm in width), and bars (6 cm tall, 5 mm thick, with widths of 7-9 mm).

Titration experiments were performed using an 18 mm tall clear plastic cylinder with a diameter of 17 mm and 1 mm thick walls. It was positioned in the center of the tank. Laboratory tubing (outer diameter 2 mm) was used to flow fluid through the cylinder. During the first scan, the cylinder contained matching fluid identical to the fluid in the tank. Twelve titrations were then performed in which the ratio of ink concentration in the cylinder to that in the tank gave an expected absorption contrast ranging from 2:1 to 64:1.

## 2.3. Theoretical background

We use the diffusion approximation to the radiative transport equation [1, 33] to model the propagation of multiply-scattered light. The approximation is valid if  $\mu_a \ll \mu'_s$ . This condition was satisfied everywhere in the experimental medium. In the diffusion approximation, the electromagnetic energy density  $u(\mathbf{r})$  inside the medium obeys the diffusion equation

$$[-\nabla \cdot D(\mathbf{r})\nabla + c\mu_a(\mathbf{r})]u(\mathbf{r}) = S(\mathbf{r}) . \quad (1)$$

Here  $D = c\ell^*/3 = c/3(\mu_a + \mu'_s)$  the diffusion coefficient,  $c$  is the average speed of light in the medium and  $S$  is the power density of the source. The diffusion equation (1) is supplemented by the boundary condition

$$u + \ell \hat{\mathbf{n}} \cdot \nabla u = 0 , \quad (2)$$

where  $\ell$  is the extrapolation distance [33, 34]. In the same limit that is required for validity of the diffusion approximation,  $D \approx c/3\mu'_s$ . Thus, if the reduced scattering coefficient  $\mu'_s$  is the same inside the target and the surrounding medium, we have  $D \approx D^{(0)} = \text{const}$ . In this case, the goal of DOT is to reconstruct  $\mu_a(\mathbf{r})$  from a set of boundary measurements of  $u(\mathbf{r})$ , assuming  $D^{(0)}$  is known. We, however, do not imply that reconstruction of  $\mu'_s(\mathbf{r})$  is not possible or not important in general. As was discussed in references [30, 31], simultaneous reconstruction of  $\mu_a$  and  $\mu'_s$  is possible with the use of either time-resolved or frequency resolved measurements.

The fast image reconstruction method described in Section 2.4 can easily be generalized to the case of heterogeneous  $\mu'_s$  [30, 31].

In our experiments, light entered the tank at the point  $\mathbf{r}_s = (\boldsymbol{\rho}_s, z_s)$ . The CCD camera measured the intensity of the beam exiting through the opposite surface at the point  $\mathbf{r}_d = (\boldsymbol{\rho}_d, z_d)$ . Here the  $z$ -axis is perpendicular to the slab, and  $|z_d - z_s| = L$  is the slab thickness, while  $\boldsymbol{\rho}_s$  and  $\boldsymbol{\rho}_d$  are the two-dimensional radius-vectors characterizing the transverse coordinates of the source and detector, respectively. The measured intensity in such an experiment,  $I(\mathbf{r}_d, \mathbf{r}_s)$ , is mathematically related to the Green's function of the diffusion equation (1),  $G(\mathbf{r}_d, \mathbf{r}_s)$ , by  $I(\mathbf{r}_d, \mathbf{r}_s) = C_d C_s G(\mathbf{r}_d, \mathbf{r}_s)$ . Here  $C_d$  and  $C_s$  are coupling constants which depend, in particular, on the extrapolation distance  $\ell$ , the transport mean free path  $\ell^*$  (see Refs. [30, 31]), and on other factors; these constants can be excluded from consideration as shown below. Note that for two arbitrary spatial arguments  $\mathbf{r}$  and  $\mathbf{r}'$  which may be either on the surface or inside the medium,  $G(\mathbf{r}, \mathbf{r}')$  can be found from the equation

$$\left[ -D^{(0)} \nabla^2 + c \mu_a(\mathbf{r}) \right] G(\mathbf{r}, \mathbf{r}') = \delta(\mathbf{r} - \mathbf{r}') \quad (3)$$

and the boundary conditions (2). We next decompose the absorption coefficient  $\mu_a(\mathbf{r})$  as  $\mu_a(\mathbf{r}) = \mu_a^{(0)} + \delta\mu_a(\mathbf{r})$ , where  $\mu_a^{(0)}$  is the constant value of the absorption coefficient in the fluid while  $\delta\mu_a(\mathbf{r})$  represents a spatial fluctuation due to the target. Then the Green's function satisfies the Dyson equation

$$G(\mathbf{r}_d, \mathbf{r}_s) = G_0(\mathbf{r}_d, \mathbf{r}_s) - \int_V G_0(\mathbf{r}_d, \mathbf{r}) c \delta\mu_a(\mathbf{r}) G(\mathbf{r}, \mathbf{r}_s) d^3 r, \quad (4)$$

where the integral is taken over the volume of the sample and  $G_0$  is the Green's function in the reference medium with  $\mu_a = \mu_a^{(0)}$ .  $G_0$  satisfies Eq. (3) with the substitution  $\mu_a(\mathbf{r}) \rightarrow \mu_a^{(0)}$  and can be found analytically in an infinite slab [30]. The left-hand side of Eq. (4) is directly measurable but  $G(\mathbf{r}, \mathbf{r}_s)$ , which appears in the right-hand side, can not be measured since the point  $\mathbf{r}$  lies inside the medium. Since  $G$  depends on  $\delta\mu_a$ , the right-hand side of (4) is, generally, a nonlinear functional of the latter. Several approximate linearization methods can be used to transform Eq. (4) to an equation which is linear in  $\delta\mu_a$ . We have used the first Rytov approximation, according to which, the right-hand side in (4) is replaced by the expression

$$G_0(\mathbf{r}_d, \mathbf{r}_s) \exp \left[ - \frac{\int_V G_0(\mathbf{r}_d, \mathbf{r}) c \delta\mu_a(\mathbf{r}) G_0(\mathbf{r}, \mathbf{r}_s) d^3 r}{G_0(\mathbf{r}_d, \mathbf{r}_s)} \right].$$

Note that this expression coincides with the right-hand side of (4) to leading order in  $\delta\mu_a$ . We then define the data function as

$$\phi(\mathbf{r}_d, \mathbf{r}_s) = -G_0(\mathbf{r}_d, \mathbf{r}_s) \ln [T(\mathbf{r}_d, \mathbf{r}_s)], \quad (5)$$

where  $T(\mathbf{r}_d, \mathbf{r}_s) \equiv I(\mathbf{r}_d, \mathbf{r}_s) / I_0(\mathbf{r}_d, \mathbf{r}_s)$  is the experimentally measurable transmission function. Here  $I_0(\mathbf{r}_d, \mathbf{r}_s)$  is the result of a measurement in a reference homogeneous medium with  $\delta\mu_a = 0$ . We then obtain the following linear integral equation:

$$\phi(\mathbf{r}_d, \mathbf{r}_s) = \int_V G_0(\mathbf{r}_d, \mathbf{r}) c \delta\mu_a(\mathbf{r}) G_0(\mathbf{r}, \mathbf{r}_s) d^3 r. \quad (6)$$

The kernel  $\Gamma(\mathbf{r}_d, \mathbf{r}_s; \mathbf{r}) = G_0(\mathbf{r}_d, \mathbf{r}) G_0(\mathbf{r}, \mathbf{r}_s)$  is known analytically and the right-hand side  $\phi(\mathbf{r}_d, \mathbf{r}_s)$  is measured experimentally. Note that we have used the fact that  $I(\mathbf{r}_d, \mathbf{r}_s) / I_0(\mathbf{r}_d, \mathbf{r}_s) = G(\mathbf{r}_d, \mathbf{r}_s) / G_0(\mathbf{r}_d, \mathbf{r}_s)$  to eliminate the coupling constants  $C_d$  and  $C_s$ . Equations (5) and (6) are the main equations of linearized DOT. The method we have used for inverting (6) is briefly described below.

## 2.4. Inversion formula

The image reconstruction method used by us is based on the translational symmetry of the slab geometry. The latter allows one to write  $G_0$  as

$$G_0(\boldsymbol{\rho}, z; \boldsymbol{\rho}', z') = \int g(\mathbf{q}; z, z') \exp[i\mathbf{q} \cdot (\boldsymbol{\rho}' - \boldsymbol{\rho})] \frac{d^2q}{(2\pi)^2}, \quad (7)$$

where the explicit expressions for  $g(\mathbf{q}; z, z')$  are given in Ref. [30]. Note, both  $g(\mathbf{q}; z, z')$  and  $G_0(\boldsymbol{\rho}, z; \boldsymbol{\rho}', z')$  are real for continuous-wave measurements. We substitute this plane-wave decomposition of  $G_0$  into (6) and take a four-dimensional Fourier transform with respect to the source and detector transverse coordinates to obtain

$$\tilde{\phi}(\mathbf{q}_d, \mathbf{q}_s) = c \int_{z_d}^{z_s} g(\mathbf{q}_s; z_s, z) g(\mathbf{q}_d; z, z_d) \delta\tilde{\mu}_a(\mathbf{q}_s + \mathbf{q}_d, z) dz, \quad (8)$$

where the Fourier-transforms are defined as

$$\tilde{\phi}(\mathbf{q}_d, \mathbf{q}_s) = \sum_{\boldsymbol{\rho}_d, \boldsymbol{\rho}_s} \phi(\boldsymbol{\rho}_d, z_d; \boldsymbol{\rho}_s, z_s) \exp[i(\boldsymbol{\rho}_d \cdot \mathbf{q}_d + \boldsymbol{\rho}_s \cdot \mathbf{q}_s)], \quad (9)$$

$$\delta\tilde{\mu}_a(\mathbf{q}, z) = \int \delta\mu_a(\boldsymbol{\rho}, z) \exp(i\boldsymbol{\rho} \cdot \mathbf{q}) d^2\rho. \quad (10)$$

With the change of variables  $\mathbf{q}_d = \mathbf{q} + \mathbf{p}$ ,  $\mathbf{q}_s = -\mathbf{p}$ , we can now re-write (8) as

$$\psi(\mathbf{q}, \mathbf{p}) = \int_{z_d}^{z_s} \kappa(\mathbf{q}, \mathbf{p}; z) \delta\tilde{\mu}_a(\mathbf{q}, z) dz, \quad (11)$$

where  $\psi(\mathbf{q}, \mathbf{p}) = \tilde{\phi}(\mathbf{q} + \mathbf{p}, -\mathbf{p})$  and  $\kappa(\mathbf{q}, \mathbf{p}; z) = cg(\mathbf{q} + \mathbf{p}; z_s, z)g(-\mathbf{p}; z, z_d)$ .

Thus, the problem has been reduced to inverting a set of linear one-dimensional integral equations with known kernels  $\kappa(\mathbf{q}, \mathbf{p}; z)$ . We do so for a discrete set of samples of the Fourier variable  $\mathbf{q}$  and then use the inverse Fourier transform to obtain  $\delta\mu_a(\boldsymbol{\rho}, z)$ . Note that Eq. (11) is inverted for each sample of  $\mathbf{q}$  by utilizing multiple discrete values of  $\mathbf{p}$ . To this end, we construct analytically the pseudoinverse to the linear integral operator of the left-hand side of (11). The mathematical details of this construction are given in Ref. [30]. Computing  $\delta\mu_a(\boldsymbol{\rho}, z)$  by the inverse Fourier transform accounting for sampling and truncation of real-space data is discussed in Refs. [25, 31]. In Ref. [31], we have considered symmetry-based image reconstruction algorithms from a more general point of view and a number of special cases have been derived, including the specific modality used in this paper (Section 3.C.1, ‘‘Fourier tomography’’).

The computational complexity of the image reconstruction algorithm described in this section is  $O(N_q N_p^3)$ , where  $N_q$  is the number of discrete values of the vector  $\mathbf{q}$ , while  $N_p$  is the number of discrete values of  $\mathbf{p}$  used to invert each one-dimensional equation (11). This is the computational cost of inverting the integral operator only. To this one should add the cost of Fourier-transforming the real-space data function and computing  $\psi(\mathbf{q}, \mathbf{p})$ . With the use of the fast Fourier transform, the latter scales as  $O(N_q^2 \ln N_q)$ . If the same amount of data and the same grid of voxels is used with a purely algebraic image reconstruction method, the computational cost of matrix inversion scales as  $O((N_q N_p)^3)$ . In the above estimate, we have assumed that the number of measurements is equal to the number of voxels. We thus see that the fast image reconstruction methods exploit the block structure of the linear operator that couples the data to the unknown function. Instead of inverting a large matrix of size  $N_q N_p$ , these methods require inversion of  $N_q$  matrices of the size  $N_p$  each, thus gaining a factor of  $N_p^2$  in computation time. We note that reconstructions which utilized data sets of up to  $10^7$  source-detector pairs required less than one minute of CPU time on a 1.3GHz workstation.

## 2.5. Simulated data

Simulated data functions for a point absorber were generated within the linear approximation by representing  $\delta\mu_a(\mathbf{r})$  as a delta-function. Data for infinite lattices of sources and detectors was computed directly in the Fourier domain using (8). For finite lattices we computed  $G_0$  numerically using (7) and substituted the result into (9); in the latter formula, summation over real space variables was truncated.

We then added noise to the data function generated for the finite lattice as follows. We expect the standard deviation due to shot noise for repeated measurements of a single source detector pair to be equal to the square root of the mean number of detected photo-electrons ( $\sigma_I(\mathbf{r}_s, \mathbf{r}_d) = \sqrt{I(\mathbf{r}_s, \mathbf{r}_d)}$ ). Propagating the error to the data function defined in equation (5) we get to first order  $\sigma_{\text{data}}(\mathbf{r}_s, \mathbf{r}_d) = \sqrt{2I_0(\mathbf{r}_s, \mathbf{r}_d) - \phi(\mathbf{r}_s, \mathbf{r}_d)}$ . We scaled both the simulated data function and the simulated reference intensity  $I_0$  to have the same maximum values as were experimentally measured. The resulting data function with shot noise was then

$$\phi_{\text{noise}}(\mathbf{r}_s, \mathbf{r}_d) = \phi(\mathbf{r}_s, \mathbf{r}_d) + \sigma_{\text{data}}(\mathbf{r}_s, \mathbf{r}_d)R. \quad (12)$$

Here  $R$  is a random variable with a Gaussian distribution and a variance of one. We note that since  $I_0 \gg \phi$ , the shot noise depends primarily on the reference intensity, not on the data function itself. In order to simulate the effect of read noise and dark current, we determined the standard deviation  $\sigma_{\text{bg}}$  of a background image taken with the light source blocked. This error was propagated as  $\sigma_{\text{data}} = \sqrt{2\sigma_{\text{bg}}^2}$ , and the resulting data function was calculated according to (12).

## 3. Experimental results

For the reconstructions shown in Fig. 1, the target was constructed of silicone rubber and shaped in the form of the letters ‘‘DOT’’ and ‘‘PENN’’. In the first experiment, we placed the letters ‘‘DOT’’ one centimeter from the source plane and the letters ‘‘PENN’’ one centimeter from the detector plane, directly behind the ‘‘DOT’’ letters. The reconstruction is shown in Fig. 1(b). The letters are clearly visible. Note that the central slice from the middle of the tank is empty, as expected. In a second experiment we placed the letters ‘‘DOT’’ in the center of the tank (the letters ‘‘PENN’’ were not present) three centimeters from source and detector planes. The reconstruction is shown in Fig. 1(c). The letters are clearly reconstructed.

In Fig. 2 we show the data used to reconstruct the images. Only data corresponding to a single source beam position is shown. For each reconstruction we show, from left to right, the reference intensity  $I_0$  when the target is not present (scattering fluid only), the intensity  $I$  when the target is present, and the Rytov data,  $\phi = -\log(I/I_0)$ , which is used in the reconstruction algorithm (see *Methods*). Note that the letters cannot be identified by simply inspecting images of the transmitted light. Structure is visible in the Rytov data when the letters ‘‘PENN’’ are close to the detector plane (Fig. 2(a)). However, when the letters ‘‘DOT’’ are in the center of the tank (Fig. 2(b)) their shape is completely blurred.

In order to quantify the transverse resolution of the reconstructed images, we prepared several bar targets from the same material described above. The bars were 7 mm to 9 mm thick and placed consecutively (one at a time) in the center of the slab. Fig. 3(a) shows the corresponding reconstructions. As the bar widths decrease, the modulation depth between bars decreases. As can be seen, all but the 7 mm bar target are well resolved. Fig. 3(b) shows reconstructions for two experiments in which the 7 mm bar target was positioned 1 cm from the source and detector planes, respectively. The bars in this figure are well resolved and the images are smoother and have fewer artifacts. As can be expected, the image is better resolved when the target is closer to the detector plane. This is because the detectors are sampled on a finer grid than the sources.

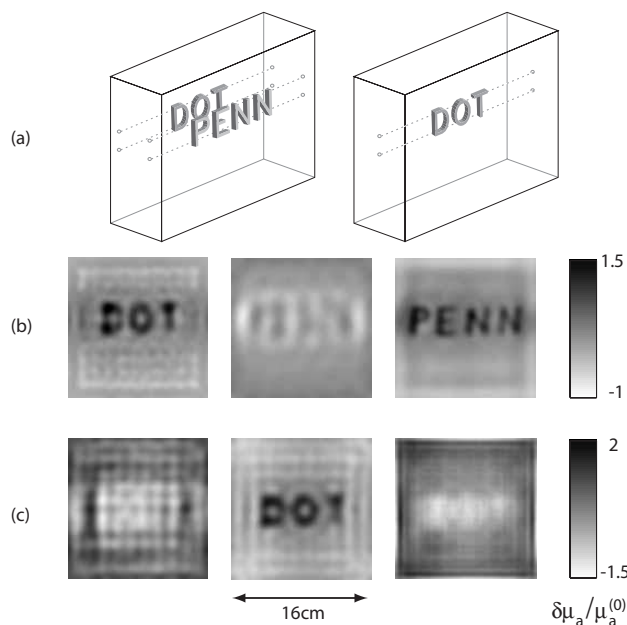


Fig. 1. Slices from three dimensional image reconstructions of the relative absorption coefficient ( $\delta\mu_a/\mu_a^{(0)}$ ) for targets suspended in a 6 cm thick slab filled with highly scattering fluid. The three slices shown for each reconstruction correspond to depths of 1 cm (left), 3 cm (middle), and 5 cm (right) from the source plane. The field of view in each slice is 16 cm  $\times$  16 cm. The quantity plotted is  $\delta\mu_a/\mu_a^{(0)}$  (a) Schematics of the positions of the letters during the experiments. Left: The target consists of letters “DOT” and “PENN”, suspended 1 cm and 5 cm from the source plane, respectively. Right: The target consists only of the letters “DOT” suspended 3 cm from the source plane, i.e., in the center of the slab. (b) Reconstructed image of the letters “DOT” and “PENN” (c) Reconstructed image of the letters “DOT”.

Experiments were also performed with bar targets having an absorption contrast of 2:1. The resulting images were very similar to those acquired with a 4:1 absorption contrast bar targets, but they contained less contrast and more noise.

The images in Fig. 3 were reconstructed using approximately  $10^7$  measurements. The effect of changing the size of the data set was investigated by sampling the detectors on a grid with a step size of 2 mm, five times larger than the minimum experimentally available detector spacing. We found that increasing the number of detectors up to the experimentally available maximum did not improve image quality. That is, reconstructions performed using 2 mm source separations or with a denser sampling of CCD pixels were visually indistinguishable from those in Fig. 3. However, *decreasing* the number of data points does result in poorer image quality, as is illustrated in Fig. 4. From left to right, three separate reconstructions of the 8 mm bar target are shown. The data for these reconstructions were taken from a single experiment with the target positioned in the center of the tank. All reconstruction parameters are kept constant, except for the number of measurements used. The reconstruction on the left uses  $8 \times 10^6$  measurements with sources and detectors sampled with 4 mm and 2 mm steps, respectively. In the center reconstruction, we use 4 mm spacing for both the sources and detectors, which corresponds to  $2 \times 10^6$  data points. In the reconstruction on the right, the sampling is 8 mm for sources and 4 mm for detectors, or, approximately,  $5 \times 10^5$  data points. It can be seen that as the number

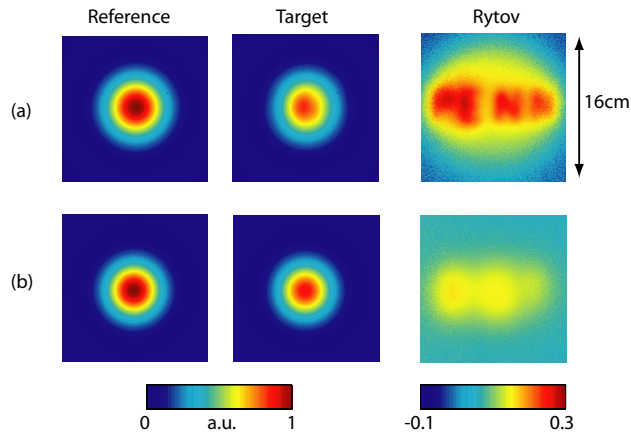


Fig. 2. Representative CCD data for the image reconstructions shown in Fig. 1. Each image corresponds to the measured light intensity for a single source beam position. The left column shows the reference intensity  $I_0$  when the target is not present (scattering fluid only). The middle column shows the intensity  $I$  when the target is present. The right column shows the Rytov data,  $\phi = -\log(I/I_0)$ , which is used in the reconstruction algorithm. (a) The target consists of the letters “DOT” and “PENN” (b) The target consists of the letters “DOT” only

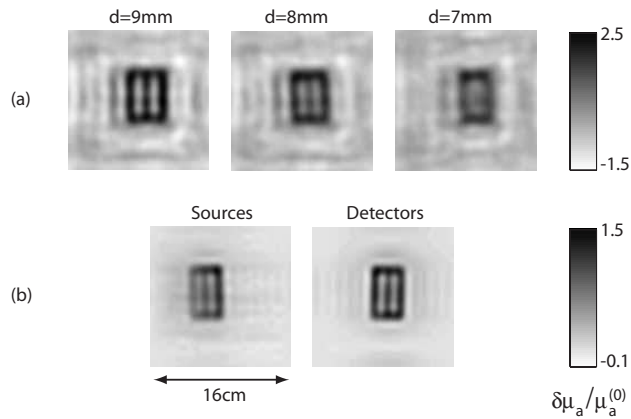


Fig. 3. Reconstructed images of bar targets. Only slices drawn at the depth of the actual target are shown. (a) 7 mm to 9 mm bar targets located in the center of the tank. Here  $d$  denotes the width of the individual bars in the targets. (b) The 7 mm bar target located 1 cm from the source (left) and detector (right) planes.

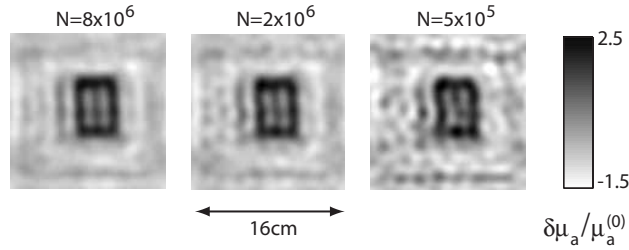


Fig. 4. Images of the 8 mm bar target from a single experiment. All reconstruction parameters are held fixed except for the number of measurements used. From left to right, correspond to  $N = 8 \times 10^6$ ,  $2 \times 10^6$ , and  $5 \times 10^5$  measurements were used for the reconstruction.

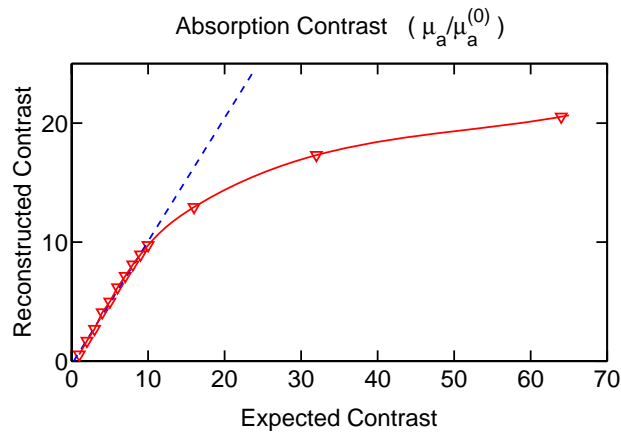


Fig. 5. Reconstructed contrast of the absorption coefficient  $\mu_a/\mu_a^{(0)}$  between the cylinder and the tank vs. the expected contrast.

of measurements decreases, image artifacts become more prominent and resolution is lost. We note that the optimal number measurements for a given experiment will vary depending on factors such as experimental geometry and noise level. For example, smaller/larger data sets would be optimal if the reconstruction field of view was smaller/larger.

To investigate the capability for quantitative reconstruction of the absorption coefficient, we have performed a titration experiment. A clear plastic cylinder was positioned in the center of the tank, and laboratory tubing was used to flow fluid through the cylinder. During the first scan, the cylinder contained scattering fluid identical to the fluid in the tank. Twelve titrations were then performed in which the ratio of ink concentration in the cylinder, to that in the tank, gave an expected absorption contrast ranging from 2:1 to 64:1. The absorption contrast, i.e., the ratio of the absorption coefficient in the cylinder to that in the surrounding fluid, was taken from the corresponding reconstructed value for a single voxel located inside the cylinder. This voxel was chosen to be the voxel with the maximum reconstructed value of the absorption coefficient for the tenth titration. In Fig. 5, the reconstructed contrast  $\mu_a/\mu_a^{(0)}$  is plotted against the expected contrast. It can be seen that the absorption is quantitatively reconstructed with a linear dependence on ink concentration over nearly a decade in absorption contrast. Deviation from linearity occurs at higher concentrations, as expected.

## 4. Discussion

### 4.1. Transverse resolution and Fourier analysis of data

Factors that limit the ability to achieve even greater spatial resolution include the finite size of the source and detector grids, the shot noise in the measured light, the noise in the CCD array (a combination of dark current and read noise), and systematic errors. The latter are errors of the model. In particular, the light transmitted through the tank is described by the diffusion equation only approximately. There are also systematic errors associated with non-ideal optics (diffraction, multiple reflections on the lens and tank surfaces). Finally, there are systematic errors associated with the nonlinearity of the inverse problem of DOT.

To better understand the dependence of transverse spatial resolution on the factors listed above, we performed the following analysis. Let all inhomogeneities be confined in a thin slice of the medium parallel to the slab,  $z_0 - h/2 < z < z_0 + h/2$ , where  $h$  is small. We seek to reconstruct the deviation of the absorption coefficient in this slice,  $\delta\mu_a(\mathbf{p}, z_0)$ , from the respective value in the surrounding fluid, as a function of the transverse variable  $\mathbf{p} = (x, y)$ . The formula (11) derived in the *Methods* Section becomes in this case

$$\psi(\mathbf{q}, \mathbf{p}) = h\kappa(\mathbf{q}, \mathbf{p})\delta\tilde{\mu}_a(\mathbf{q}, z_0).$$

Here  $\psi(\mathbf{q}, \mathbf{p})$  is the measurable data function,  $\kappa(\mathbf{q}, \mathbf{p})$  is known analytically (see *Methods* for precise definitions of  $\psi$  and  $\kappa$ ), and  $\delta\tilde{\mu}_a(\mathbf{q}, z_0)$  is the transverse Fourier transform of  $\delta\mu_a(\mathbf{p}, z_0)$  with respect to  $\mathbf{p}$ . The real-space function  $\delta\mu_a(\mathbf{p}, z_0)$  is obtained by inverse Fourier transformation, namely,

$$\delta\mu_a(\mathbf{p}, z_0) = \frac{1}{h} \int \exp(i\mathbf{q} \cdot \mathbf{p}) \frac{\psi(\mathbf{q}, \mathbf{p})}{\kappa(\mathbf{q}, \mathbf{p})} \frac{d^2q}{(2\pi)^2}.$$

The choice of  $\mathbf{p}$  in the above formula is arbitrary since the problem is overdetermined (we use four-dimensional data to reconstruct a two-dimensional function); it is sufficient to choose  $\mathbf{p} = 0$ . We then use the data function  $\psi(\mathbf{q}, 0)$  for reconstruction. The latter is taken from experiment and contains noise. It is important to note that the “ideal” data function is rapidly (exponentially) decreasing with  $|\mathbf{q}|$ . However, the experimental noise is approximately white, i.e., the amplitude of its Fourier transform is approximately constant in the range of  $|\mathbf{q}|$  which is of interest. In image reconstruction, integration in the above formula is over a disc  $|\mathbf{q}| < q_{\max}$  such that outside of this disc, the signal-to-noise ratio in  $\psi(\mathbf{q}, 0)$  becomes smaller than unity. It then follows that the minimum spatial feature that can be resolved has a characteristic transverse dimension of  $\Delta x \sim \pi/q_{\max}$ .

A few comments on the above analysis are necessary. First, if the target is not confined to a thin slice, the transverse resolution can only be lower than the estimate  $\pi/q_{\max}$ . Second, one can attempt to use additional degrees of freedom (i.e.,  $N$  distinct values of  $\mathbf{p}$ ) to improve the resolution. This approach, however, is not expected to yield a significant improvement since the noise amplitude decreases no faster than  $1/\sqrt{N}$ , while the function  $\psi(\mathbf{q}, \mathbf{p})$  decreases exponentially with  $|\mathbf{q}|$ .

To illustrate the above resolution estimate, we plot in Fig. 6 the power spectrum of the data for a point absorber located in the center of the tank. The data function  $\psi(\mathbf{q}, 0)$  is in this case cylindrically symmetric and we can write  $\psi(\mathbf{q}, 0) = \Psi(q)$ , where  $q = |\mathbf{q}|$ . The five curves shown in Fig. 6 contain (i) simulated ideal data corresponding to infinitely large and dense grids of noiseless sources and detectors, (ii) simulated data (without noise) for the finite grids of sources and detectors that were used in the experiments, (iii) simulated data for the finite grids with

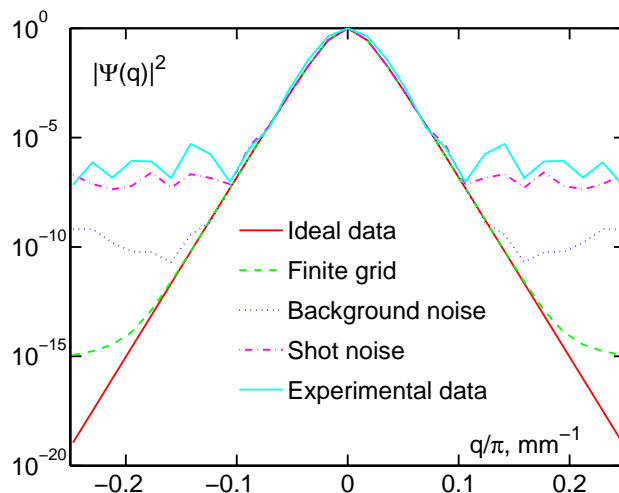


Fig. 6. Power spectra of the data function  $|\Psi(q)|^2$  (defined in the text) for a small absorber located in the center of the tank. The different curves correspond to simulated ideal data, simulated data from finite grids of sources and detectors, simulated data with background noise, simulated data with shot noise, and to experimental data, as indicated.

background noise added (i.e. Gaussian distributed noise with a variance equal to the variance of the detected signal when the laser is off), (iv) simulated data for the finite grid with shot noise added (i.e. Gaussian distributed noise with a variance equal to the number of photoelectrons detected experimentally), and (v) data from an experiment with a small (4 mm) highly absorbing target in the tank (see *Methods* for details of the simulations). The early onset of noise in the simulated data with shot noise, suggests the latter is the limiting factor in our experiments. We thus conclude that the other errors discussed above (e.g. the finite numbers of sources and detectors, CCD noise, errors in the diffusion model, non-ideal optics, and non-linearity) do not play a significant role in limiting image resolution. We see that noise begins to dominate the data at  $q_{\max}/\pi \approx 0.1 \text{ mm}^{-1}$ . This corresponds to a spatial resolution of  $\lesssim 1 \text{ cm}$ . For objects closer to the surface, the power spectrum decays more slowly. For example, for a point absorber located 1 cm from the surface, shot noise begins to dominate the data at  $q_{\max}/\pi \approx 0.25 \text{ mm}^{-1}$ , which corresponds to a spatial resolution of  $\lesssim 4 \text{ mm}$ .

#### 4.2. Titration experiments

The saturation effect seen in Fig. 5 can be explained as follows. When the absorption of the target is very high, most of the light is absorbed as soon as it enters the target and almost no light reaches its interior; the absorption coefficient of the interior can be arbitrarily changed with no significant effect on the measured signal. This is a manifestation of the nonlinearity of the inverse problem of DOT. Note that the onset of nonlinearity in Fig. 5 occurs at absorber concentrations which are well beyond the range of contrast encountered in biological tissues. We finally note that the nonlinearity becomes stronger when the absorbing target becomes larger, as less and less light can penetrate the interior.

### 5. Conclusion

We have obtained high quality, quantitatively accurate, reconstructed images of complex structures deeply embedded in highly-scattering media. This result was achieved by using both a

non-contact scanner capable of collecting large amounts of data and a fast image reconstruction algorithm capable of utilizing this data. We expect that these techniques will greatly improve the utility of diffuse optical methods in biomedical imaging.

### **Acknowledgments**

This research was supported, in part, by the NIH grants R01-CA75124, R01-EB-002109, NTROI 1U54CA105480, P41RR02305, R21EB004524, R01-EB-004832 and by the NSF under grants DMS-0554100 and EEC-0615857.